Meteosat-Based Characterization of the Spatiotemporal Evolution of Warm Convective Cloud Fields over Central Europe

SEBASTIAN BLEY, HARTWIG DENEKE, AND FABIAN SENF

Leibniz Institute for Tropospheric Research, Leipzig, Germany

ABSTRACT

The spatiotemporal evolution of warm convective cloud fields over central Europe is investigated on the basis of 30 cases using observations from the Spinning Enhanced Visible and Infrared Imager (SEVIRI) on board the geostationary Meteosat platforms. Cloud fields are tracked in successive satellite images using cloud motion vectors. The time-lagged autocorrelation is calculated for spectral reflectance and cloud property fields using boxes of 16×16 pixels and adopting both Lagrangian and Eulerian perspectives. The 0.6-μm reflectance, cloud optical depth, and water path show a similar characteristic Lagrangian decorrelation time of about 30 min. In contrast, significantly lower decorrelation times are observed for the cloud effective radius and droplet density. It is shown that the Eulerian decorrelation time can be decomposed into an advective component and a convective component using the spatial autocorrelation function. In an Eulerian frame cloud fields generally decorrelate faster than in a Lagrangian one. The Eulerian decorrelation time contains contributions from the spatial decorrelation of the cloud field advected by the horizontal wind. A typical spatial decorrelation length of 7 km is observed, which suggests that sampling of SEVIRI observations is better in the temporal domain than in the spatial domain when investigating small-scale convective clouds. An along-track time series of box-averaged cloud liquid water path is derived and compared with the time series that would be measured at a fixed location. Supported by previous results, it is argued that this makes it possible to discriminate between local changes such as condensation and evaporation on the one hand and advective changes on the other hand.

1. Introduction

Warm convective clouds are highly variable in space and time and cover large areas of Earth (Turner et al. 2007). Through the transport of energy and moisture, they couple the boundary layer and the free troposphere. Their bright cloud tops reflect the incoming sunlight, which strongly modulates the atmospheric radiation budget (Trenberth et al. 2009). Because of our lack of understanding of relevant processes and feedbacks, low-level clouds remain a dominant source of uncertainty in climate projections (Clement et al. 2009).

The central motivation of this study is to find suitable techniques and quantities that allow a spatiotemporal characterization of convective cloud fields and their life cycle from space, and can subsequently serve, for example, as metrics for evaluating parameterizations of cumulus convection in climate models (Dorrestijn et al. 2013). This characterization provides complementary information about the spatial structure and temporal changes of cloud properties to serve as a fingerprint of underlying dynamical and microphysical processes. In addition, information on the spatial structure of cloud fields as given by the power spectrum are essential to realistically represent cloud radiative effects in models and observations (Davis et al. 1996).

In an early global study based on satellite observations, the frequency of fractional cloudiness on scales smaller than 50–200 km^2 was found to be 20%–30% (Rossow and Garder 1993). Albrecht (1989) already pointed out the high uncertainties of the global albedo in climate models due to the crude representation of

---

Corresponding author address: Sebastian Bley, Remote Sensing of Atmospheric Processes, Leibniz Institute for Tropospheric Research, Permoserstr. 15, Leipzig, Germany.
E-mail: bley@tropos.de

cumulus cloud coverage, which still affect current models. It has been suggested that intercomparisons of observations, large-eddy simulations (LES), and single-column models (SCM) are essential for improving such parameterizations (Lenderink et al. 2004). Brown et al. (2002) designed a LES model of shallow cumulus convection over land as basis for testing cloud parameterizations in numerical weather prediction and climate models. High-resolution models, however, also have problems in representing clouds realistically, as can be determined by comparisons with observations. In recent years the spatiotemporal resolution of models has been steadily increased to better resolve relevant small-scale cloud processes. One promising source of observations for the evaluation of high-resolution models is meteorological satellites because of their global coverage. In contrast to polar-orbiting satellites, geostationary satellites like Meteosat have the capability to observe and track cumulus clouds from their early developing stage onward and are the focus of the present study.

Separating cloudy from cloud-free areas is an essential first step in the retrieval of cloud physical properties from satellite. Roebeling et al. (2006) developed an algorithm to retrieve the cloud optical thickness (τ), the cloud droplet effective radius (r_e), and the liquid water path (LWP) from solar channels during daytime. However, the investigation of warm convective cloud fields based on these retrieved properties is challenging because of low LWP values and small clouds sizes. Fractional cloudiness induces small-scale optical property variations and thus high uncertainties (Han et al. 1994). This can be explained by small clouds and cloud-free areas that are smaller than the actual satellite resolution (Koren et al. 2008). In particular the retrieval of r_e is very sensitive to the spatial satellite resolution. Wolters et al. (2010) identified that r_e is highly overestimated at lower satellite resolutions because of variability and the nonlinear relation between the absorbing reflectances and r_e. These uncertainties also propagate to estimates of the LWP, which is generally assumed to be proportional to the product of τ and r_e (Horvath et al. 2014).

These cloud property uncertainties demonstrate that validation of cloud property retrievals with ground-based or other satellite measurements is required (Roebeling et al. 2008). However, comparing convective cloud properties obtained from satellite with instantaneous ground-based measurements is challenging because of their rapid changes in space and time (Feijt and Jonker 2000; Deneke et al. 2009). Despite these uncertainties, Meteosat observations are the best available option to characterize the spatiotemporal evolution of cloud fields over Europe, and thus offer unique reference data for model evaluation. Up to now, however,

this potential has not been fully exploited, also because of the lack of established techniques and quantities for such an evaluation.

In prior studies, Cahalan et al. (1982) performed a spatiotemporal statistical analysis of day-to-day changes in cloudiness using data from the scanning radiometer aboard the polar-orbiting National Oceanic and Atmospheric Administration satellites. They calculated characteristic time and length scales from decorrelation functions of time- and space-lagged infrared (IR) images and showed that Lagrangian correlation times are always larger than the Eulerian. They, however, focused on relatively large spatial and temporal scales on the order of several hundred kilometers and several days, respectively. For the characterization of statistical cloud properties on a kilometer scale, Slobodda et al. (2015) investigated decorrelation lengths for different measurements in the solar and IR part of the spectrum over Europe and using Meteosat observations. They stated that visible and near-IR observations, which are basis for cloud property retrievals, decorrelate much faster than IR fields, which are related to cloud-top temperature and obtain their signals from higher atmospheric layers. Feijt and Jonker (2000) showed that temporal scales of variability in LWP derived from ground-based microwave measurements can be matched to spatial scales in satellite-retrieved fields of LWP.

A spatiotemporal characterization of convective cloud fields does potentially have, however, a wide applicability, ranging from forecasts of solar irradiance in the context of solar power generation (Hammer et al. 1999) to the detection of convective initiation (Senf et al. 2015). Toward this, the Eulerian perspective and the Lagrangian perspective will be contrasted. While the former is typical for ground-based measurements, we argue that the latter is better suited for a process-based characterization of clouds, as it allows a separation of advective and convective changes. Taking these findings into account has high implications for observation networks. We also aim for the identification of quantities that are suitable for model comparison. We therefore consider not only Meteosat reflectances but also optical and microphysical cloud properties and high-resolution wind data. Here, the temporal changes of satellite-derived LWP fields receive particular attention in our correlation analysis because LWP is readily available from models, and changes can be attributed to physical processes affecting condensation and evaporation of cloud droplets. Please note that precipitation and glaciation processes also influence the evolution of LWP fields; however, they are not considered in our study.
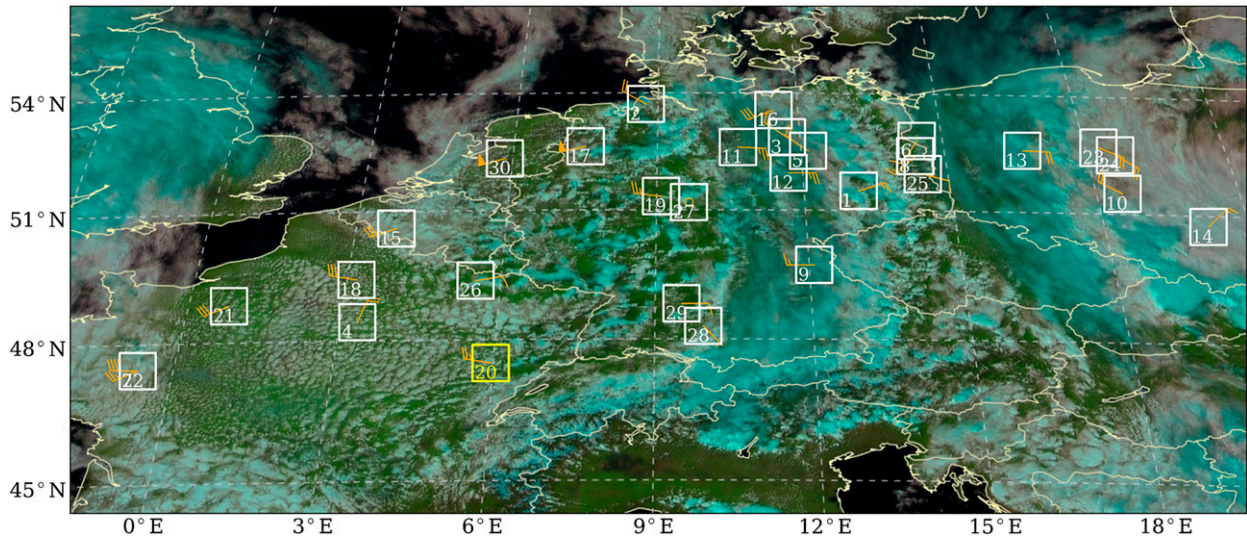
FIG. 1. Overview map of the selected cases. The underlying RGB image (Lensky and Rosenfeld 2008) is a composite of the 0.6-, 0.8-, and 1.6-μm channels and the HRV channel from MSG SEVIRI showing the cloud scene of case 20 at 1200 UTC 17 May 2012. The white rectangles indicate the track starting area along with the number of the trajectory. The orange barbs illustrate the cloud motion vectors for the respective case. Note that the cloud scenery is different for each of the cases except case 20.

Section 2 provides an overview of the data, and section 3 describes our main methodology for the study. In section 4, we present the results and discuss how they relate to similar past studies. Section 5 summarizes conclusions and gives suggestions for future studies.

2. Data

Data from the Spinning Enhanced Visible and Infrared Imager (SEVIRI) are used in this analysis. This optical imaging radiometer is the main payload on board the geostationary Meteosat Second Generation (MSG) satellites, which are operated by EUMETSAT. In addition to 11 narrowband channels (solar and IR) with a nadir spatial resolution of $3 \times 3 \, \text{km}^2$, one broadband high-resolution visible (HRV) channel ($1 \times 1 \, \text{km}^2$ in nadir) is applied. A detailed technical description of MSG is given by Schmetz et al. (2002).

For this paper, 30 cases from the years 2012 and 2013 have been selected from Meteosat's rapid-scan service (RSS) covering Europe with a 5-min repeat cycle from a satellite position at 9.5°E above the equator. The cases show low-level broken cumulus clouds in different meteorological environments. Detailed information about the meteorological conditions can be found in section 4a. *Meteosat-8* provided this service until 9 April 2013, when it was replaced by *Meteosat-9*. Our domain of interest covers Germany and parts of eastern, western, and central Europe (Fig. 1). The white rectangles indicate the starting box of each track,

which is labeled with a track number. Because of the viewing geometry of Meteosat, the box area varies from approximately $50 \times 110 \, \text{km}^2$ in the north to $50 \times 90 \, \text{km}^2$ in the south of the domain. The orange barbs represent the calculated cloud motion velocity (CMV) and direction. In the center of our domain, one pixel has a sampling size of about 6 km (northward) by 3.6 km (eastward) and 2 km (northward) by 1.2 km (eastward) for the narrowband channels and the HRV channel, respectively.

For the analysis, the EUMETSAT Satellite Application Facility on Support to Nowcasting and Very Short Range Forecasting (NWC SAF) software package (Derrien and Le Gléau 2005) was used together with the KNMI cloud physical properties (CPP) retrieval (Roebeling et al. 2006), which has been developed in a framework of the Satellite Application Facility on Climate Monitoring (CM-SAF; Schulz et al. 2009). With the NWC SAF software, the cloud mask (CMa), cloud type (CT), cloud-top height (CTH), and high-resolution wind (HRW) products have been derived. The quantities τ, r_e, and LWP have been retrieved for cloudy pixels with CPP; τ and r_e retrievals use simulated lookup tables for cloudy 0.6- and 1.6-μm reflectances and are described in more detail in Roebeling et al. (2006). All these cloud properties except the HRW product ($1 \times 1 \, \text{km}^2$) have the MSG standard resolution of $3 \times 3 \, \text{km}^2$. The estimation of cloud properties within CPP assumes a vertically homogeneous cloud. However, observations of shallow cumulus clouds indicate

a linear increasing liquid water content (LWC) with height within the cloud (Nicholls and Leighton 1986). Since the focus of this study is the characterization of warm convective clouds, the relation

$$\text{LWP} = \frac{5}{9}\rho_w \tau \times r_e \qquad (1)$$

is used to estimate the LWP, assuming adiabatic clouds where ρ_w is the density of liquid water [see Wood and Hartmann (2006) for further discussion]. As a fourth cloud-field variable, the cloud droplet number concentration can be expressed as

$$N_d = \alpha \tau^{0.5} \times r_e^{-2.5}, \qquad (2)$$

assuming adiabatic clouds with a monotonic increasing LWC and r_e (Quaas et al. 2006). The constant $\alpha = 1.37 \times 10^{-5}\,\text{m}^{-0.5}$ as given by Brenguier et al. (2000) is used in our study.

The selected cases show a high degree of spatial cloud variability. Cloudy pixels might indeed contain partially cloud-free regions in the subpixel range that are smaller than SEVIRI's narrowband spatial resolution (Roebeling et al. 2006). Consequently, SEVIRI's narrowband observations as well as retrieved cloud products might be strongly affected by this subpixel variability (Deneke et al. 2009; Wolters et al. 2010). Because of the coarse spatial resolution of MSG, τ is usually underestimated while r_e is generally overestimated. This effect depends on viewing geometry (e.g., Horvath et al. 2014) and becomes even more pronounced for broken cumulus clouds (Wolters et al. 2010; Marshak et al. 2006). The resulting cloud property uncertainties and biases are not further investigated or corrected for this study. Instead, we focus on the characterization of the cloud-field structure as well as the spatiotemporal evolution of cloud properties. Both processes reduce the autocorrelation between space and time-lagged cloud fields.

Shallow cumulus clouds cannot be detected from Meteosat in their early initiation phase because of the limited sensor resolution. Even cumulus mediocris or congestus are oftentimes smaller than the area probed by a standard-resolution Meteosat pixel ($\approx 20\,\text{km}^2$). For that reason, we additionally make use of the HRV channel, which covers a pixel area of 1.9–$2.4\,\text{km}^2$ in our domain. Furthermore, a high-resolution visible cloud mask (HRV-CMa) is calculated to separate between cloudy and cloud-free regions and to improve the case selection (Bley and Deneke 2013). We eliminate all cases where the CT products detect ice clouds and assume nonprecipitating cloud fields, because rain formation mainly involves ice-related processes in our domain.

3. Method

a. Cloud-field tracking

Because of the relatively coarse spatial resolution of MSG, we are not able to derive characteristics representative of single cumulus clouds. Instead, we determine the statistics of a spatially extended convective cloud field within a selected box. To get a sufficient number of pixels representative of a cloud field, we analyze boxes containing convective clouds within an area of 16×16 low-resolution or 48×48 HRV pixels [$\sim(60 \times 96)\,\text{km}^2$]. The cloud fields are tracked temporally through successive satellite images from MSG. This is done in a two-step procedure.

Initially, the NWC SAF HRW product is calculated and used as a first guess of the horizontal wind (García-Pereda 2013). This product is based on a cross-correlation method and contains atmospheric motion vectors (AMVs) for pixels that are characterized by particular tracers (e.g., cloud edges) that can be matched in subsequent satellite images. We have adapted the default configuration files of the algorithm to get more motion vectors representative for the motion of low-level broken clouds, which are normally rejected by the stringent quality tests of operational AMV products (Bedka and Mecikalski 2005). Details can be found in appendix A, including the configuration file that is contained in the online supplemental material. To also consider slow cloud motions, the shortest possible time interval of 10 min is chosen. The most important input to the HRW product for our applications is the HRV channel, as the low-resolution channels are not able to properly resolve the cloud edges of small convective clouds. The output of the HRW product contains all AMVs that are found in a specific height level. We average all AMVs within our area of interest for each height level. This mean AMV yields the direction and shift within a 10-min time interval that is applied to the central pixel of the box. To identify the height level that represents the cloud-field motion best, the autocorrelation between the actual and shifted box is calculated for each level (see section 3b). The AMV that yields to the highest autocorrelation is then chosen for the tracking. The optimal AMV is divided by a factor of 2 to obtain the displacement of the cloud field at full 5-min resolution. The motion vectors are then assembled for different time steps to obtain a trajectory offering a Lagrangian perspective of the evolving cloud field (Fig. 2). As a final quality check, we tested whether the decorrelation time for the field within an Eulerian box
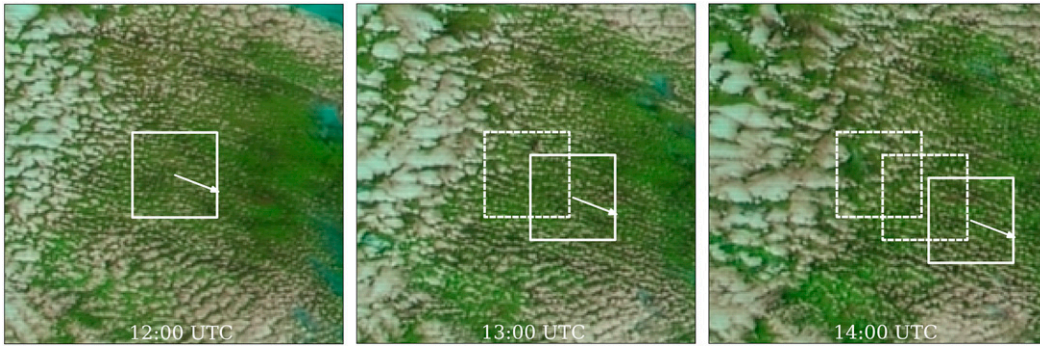
FIG. 2. Illustration of a 48 × 48 box that moves along its trajectory. The white arrow indicates the direction and distance for the next center of the box, starting from the center of the previous box.

is higher than that along the Lagrangian trajectory. This happens if the mean cloud motion is so small that it cannot be accurately quantified by AMVs, which are limited to integer pixel resolution. In this case, a neighboring box yielding a higher autocorrelation for a time lag of 30 min is sought. If such a box is found, it is used to redefine the trajectory.

b. Autocorrelation for successive cloud fields

The autocorrelation function r that describes the similarity of successive cloud fields is used in this study to quantify the temporal persistence of cloud structures and is used as basis of our spatiotemporal analysis of clouds fields. To avoid edge effects on the box sides, the cloud fields are multiplied by a normalized Hamming window filter function.

The autocorrelation function is calculated in three different ways. First, it is calculated as time-lagged autocorrelation function for a fixed box (Euler), then along the cloud motion trajectory (Lagrange), and also for a fixed time but for different discrete displacement vectors in x and y directions to obtain the spatial autocorrelation. Figure 3 illustrates schematically how the box shifts are applied. The scheme is plotted in two dimensions collapsing the two spatial dimensions into one for easier visualization. However, the spatial box shift is not only performed in the x direction but also in the y direction.

Each Lagrangian trajectory consists of $N = 24$ motion vectors that connect the 25 box centers to form a 2-h track with a time resolution of $\Delta t = 5$ min. For a time lag of $k\Delta t$, the average autocorrelation is defined as

$$R_k = \frac{1}{N-k} \sum_{n=1}^{N-k} r(n, n+k) \qquad (3)$$

for successively determined autocorrelation functions $r(n, n+k)$ correlating the cloud field at time $n\Delta t$ with the field at $(n+k)\Delta t$. The average autocorrelation function

R_k represents a robust measure of the temporal persistence of a cloud field and reduces statistical variations. For the calculation of Eulerian and Lagrangian decorrelation times, time lags up to $k = 12$, that is, up to 60 min, are considered. For the determination of decorrelation lengths, a maximum pixel shift in row- or columnwise direction of $k = 10$ is applied.

c. Decorrelation time and length

The autocorrelation as function of time lag or pixel shift typically has been found to follow an exponential decay with sufficient accuracy for our purposes.
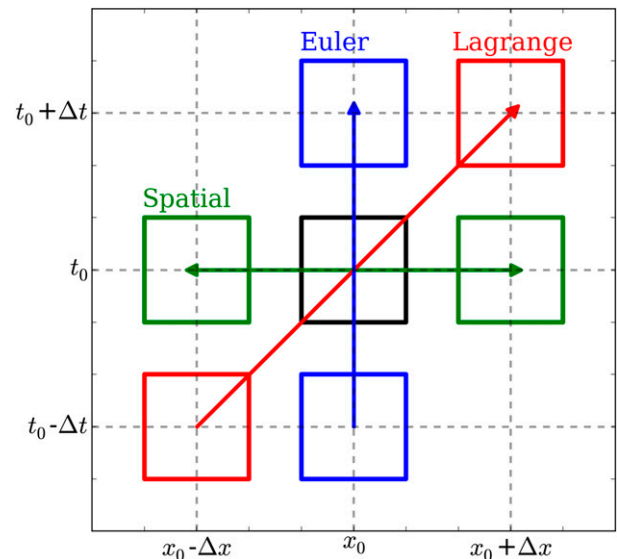

FIG. 3. Schematic diagram illustrating the way by which the Lagrangian, Eulerian, and spatial autocorrelations are applied with respect to time and space dimensions. The arrows indicate the box shift for the different approaches with constant location but varying time (blue), constant time but different spatial shifts (green), and varying time and location (red) related to the cloud-field tracks.

Therefore, the average Eulerian autocorrelation $R_{k,E}$, the average Lagrangian autocorrelation $R_{k,L}$, and the average spatial cross-correlation $R_{k,S}$ are approximated by

$$R_{k,E} = e^{-(k\Delta t)/\tau_{D,E}}, \tag{4}$$

$$R_{k,L} = e^{-(k\Delta t)/\tau_{D,L}}, \quad \text{and} \tag{5}$$

$$R_{k,s} = e^{-(k\Delta x)/\lambda_{D,x}}, \tag{6}$$

where Δt and Δx represent the time step of 5 min and spatial distance of a pixel shift, respectively. The quantities $\tau_{D,E}$, $\tau_{D,L}$, and $\lambda_{D,x}$ stand for the characteristic time and space scales at which the convective cloud field has substantially changed its structure from its initial pattern. A similar definition of characteristic scales was applied by Cahalan et al. (1982). Practically, the Eulerian ($\tau_{D,E}$), and Lagrangian ($\tau_{D,L}$) decorrelation times as well as the decorrelation lengths (λ_D) are calculated as the intersection between the e^{-1} line and the linear fit between $R_k > e^{-1}$ and $R_k < e^{-1}$.

The simplest statistical model yielding the described decorrelation behavior is an autoregressive process of first order (Von Storch and Zwiers 2002), which describes a noise-driven system with some persistence. More complex statistical models, like an autoregressive process of second order, will exhibit a different decorrelation function and might ultimately better describe the observations. This has, however, not been pursued in our study and is left for future research.

4. Results and discussion

In this section, we quantify the statistical parameters for all analyzed cases including their uncertainties. Relevant satellite attributes that influence the spatiotemporal characteristics of warm convective cloud fields are discussed. In section 4d, we present two case studies and their associated LWP time series including a separation between advectively and convectively induced changes of their field-averaged LWP.

a. Meteorological conditions

In total, 30 cases were selected in the period from April to August from the years 2012 and 2013. The spring and summer period is chosen because of favorable meteorological conditions for warm convective clouds over central Europe. The cases are characterized by different environmental conditions with respect to the cloud motion velocity and direction, synoptic situation, and cloud extent. (An overview of all tracked convective cloud fields, including the exact time and the meteorological conditions, is given in Table B1 in appendix B.)

Additionally the calculated characteristic spatiotemporal scales are included. All cloud fields are analyzed for 2 h covering the early afternoon, which is usually the time of day with the highest convection potential.

Four example cloud fields are shown in Fig. 4. Figures 4a and 4b show convective clouds forming in postfrontal cloud air conditions connected with relatively high wind speeds over northern Germany (Fig. 4a) and Poland (Fig. 4b). Both examples indicate homogeneous cloud patterns lateral to the wind direction. In contrast, Figs. 4c and 4d demonstrate example scenes with slow wind speeds with no constant wind directions.

In central Europe, warm convective cloud fields typically develop after the passage of cold fronts connected with low pressure systems when cold and humid air is advected from the Atlantic Ocean and North Sea (cases 2–8, 10, 15–22, 30). Because of large-scale horizontal advection of humid air, these cloud fields are sometimes stable over long distances ($\sim$100 km). Warm convective cloud fields with very low average cloud motions (CMV < 5 m s^{-1}) mainly occur in warm sectors or prefrontal conditions with low horizontal gradients (cases 9, 25–29). This leads to the initiation of convective clouds that can grow into deep convective systems (Senf et al. 2015). The other cases (1, 11–14, 23, 24) are associated with low pressure systems over southern and eastern Europe.

The spatial distribution of LWP, τ, r_e, and N_d for one selected case over Poland on 19 May 2013 is visualized in Fig. 5. The convective cloud field formed around noontime in southeasterly warm air advection due to a low pressure system over Italy. Moderate-speed CMVs were observed with 5.5 m s^{-1} in the x direction and 6 m s^{-1} in the y direction. The LWP field exhibited a spatial decorrelation length of 8 km in the north–south direction and 6.5 km in the east–west direction. All cloud properties are estimated at SEVIRI's standard resolution with a typical pixel area of 21 km^2. To illustrate the large subpixel variability in these cloud scenes, a semitransparent overlay of a high-resolution red-green-blue (RGB) image is used in Fig. 5. In general, cloudy pixels that are considered by the CPP retrieval might contain cloudy and cloud-free areas. Consequentially τ and LWP are usually underestimated, while r_e is overestimated (Coakley et al. 2005; Jonkheid et al. 2012). However, the LWP uncertainty is likely still smaller for these broken liquid water cloud fields than that for mixed-phase clouds (Jonkheid et al. 2012). As mentioned before, we do not elaborate on these uncertainties, which have been extensively studied in the scientific literature (e.g., Zinner and Mayer 2006). Instead, we focus here on the question whether they are well suited to characterize the temporal evolution of
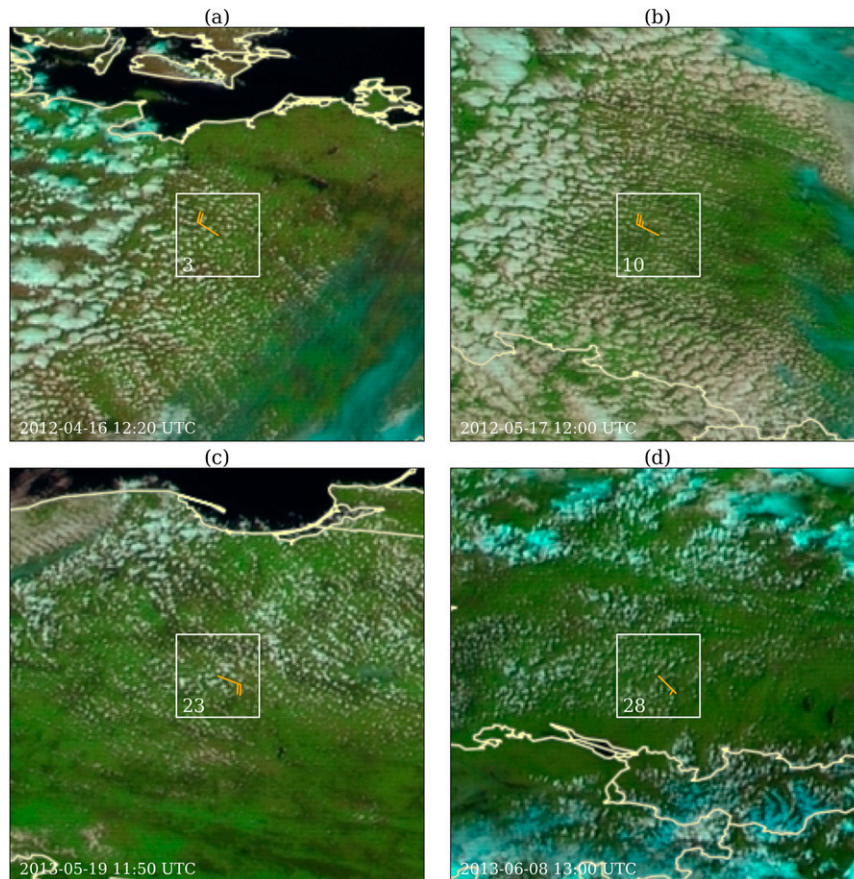
FIG. 4. Four selected cases displayed with the same markers as in Fig. 1, but magnified. The RGB images show postfrontal cases over (a) Germany and (b) Poland, (c) a case over Poland that is associated with a low over southern Europe, and (d) a case for a scattered cloud field over southern Germany in a low horizontal wind gradient environment.

cloud fields and allow a more physically based description than that offered by radiances.

b. Comparison of radiances and cloud properties with respect to their correlation behavior

In this section, we present the decorrelation times obtained for the different spectral reflectance channels of MSG and compare them to those found for various retrieved cloud properties. This analysis is done to determine the temporal persistence of the different parameters. Furthermore, we demonstrate the reliability of our cloud-field-tracking method.

The following results are based on Eq. (3) and calculated for the Lagrangian tracks (listed in Table B1). As described earlier, these tracks are based on the NWC SAF HRW motion vectors, which are mainly calculated from HRV reflectance images. Figure 6 contrasts the Eulerian (Fig. 6a) and Lagrangian (Fig. 6b) autocorrelation function for the 0.6-μm channel, the 0.8-μm channel, the HRV channel, and a coarse-grained HRV channel.

The coarse-grained HRV channel has been obtained from the standard HRV channel by averaging 3×3 pixels to approximate the standard MSG horizontal resolution. This averaging has been performed to test the sensitivity of the decorrelation time to spatial resolution.

At this point, we caution that 30 cases might be too few to assess whether some of the smaller differences in the average decorrelation times are statistically significant. However, larger differences are likely robust, especially those found when contrasting the decorrelation times for different cloud properties.

The average decorrelation times for all spectral channels are nearly 2 times longer for the Lagrangian than for the Eulerian perspective. Regardless of the perspectives, the 0.6-μm channel shows the highest decorrelation times, while the HRV channel exhibits rather low values. This is likely caused by the threefold higher spatial resolution of the HRV channel, which better resolves small-scale variability in the inhomogeneous structure of convective cloud fields. If this small-scale and evidently short-lived
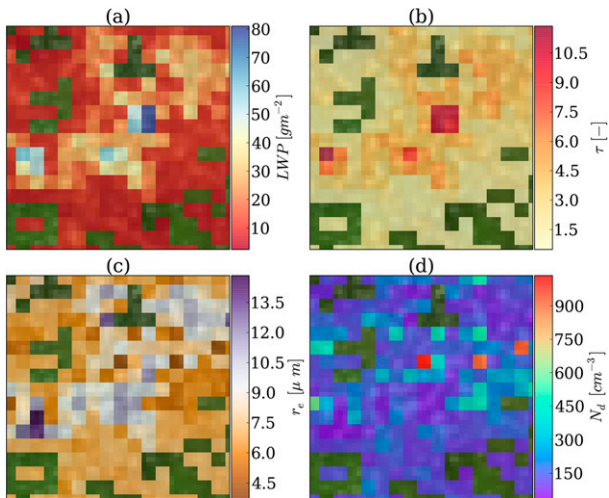
FIG. 5. Two-dimensional fields of cloud properties for case 23 on 19 May 2013 over Poland. The RGB composite is plotted in the background. Illustrated are (a) LWP, (b) τ, (c) r_e, and (d) N_d. While the cloud properties contain only 16×16 low-resolution pixels, the underlying RGB image involves 48×48 HRV pixels.
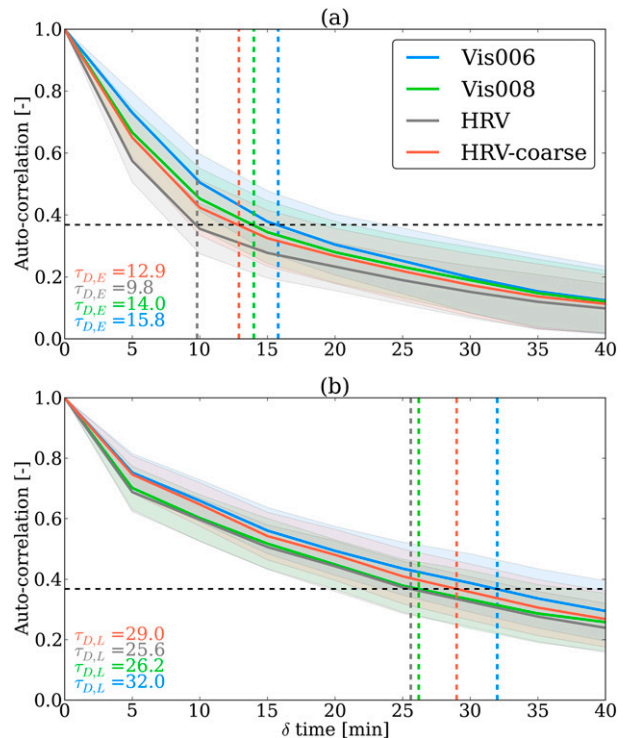

FIG. 6. (a) Eulerian and (b) Lagrangian autocorrelation function averaged for all cases and applied to MSG's standard visible channels 0.6 and 0.8 μm, the HRV channel, and an additional coarse-grained HRV channel with MSG's standard resolution. The shaded areas illustrate the standard deviation, and the dashed vertical lines show the decorrelation times τ_D for the four channels. The horizontal black line marks the decorrelation threshold.

cloud variability is removed by smoothing to lower resolution, an increase in the temporal autocorrelation is found. As the broadband spectral response of the HRV channel overlaps the response functions of the 0.6- and 0.8-μm channels, the temporal autocorrelation of the HRV channel is expected to lie between that of both narrowband channels. This is in fact observed, with a Lagrangian decorrelation time for the coarse-grained HRV channel of 31 min, which lies between $\tau_{D,L(0.8\mu m)}$ (27.7 min) and $\tau_{D,L(0.6\mu m)}$ (33.2 min). In the Eulerian perspective, the relatively higher $\tau_{D,E(0.8\mu m)}$ is likely caused by stationary patterns in the underlying surface reflectance caused by the strong reflectance of vegetation at 0.8-μm wavelength.

In the next step, the correlation analysis is repeated for different cloud properties of the convective cloud fields. The result for τ, r_e, LWP, and N_d is shown in Fig. 7. We have additionally added the autocorrelation of the 0.6-μm reflectance as reference. In both perspectives, the correlation functions of the 0.6-μm reflectance and τ show the best results and are hardly distinguishable. This is expected, because the retrieval of τ is highly dependent on the 0.6-μm reflectance (Nakajima and King 1990; Roebeling et al. 2006) and therefore shares similar spatial statistics. The shortest decorrelation times are found for N_d and r_e, with both decorrelating faster than 20 min. It remains unclear whether this behavior is physically caused or is attributable to uncertainties in the retrievals. In contrast, $\tau_{D,L(\text{LWP})}$ (31 min) lies in a similar range with $\tau_{D,L(\tau)}$ (34.1 min) and $\tau_{D,L(0.6\mu m)}$ (33.2 min). The shaded areas demonstrate a high standard deviation

of approximately ±5 min, which has been determined from the case-to-case variations. In conclusion, even besides possible shortcomings in the retrievals of cloud properties due to subpixel variability, the structures of τ and LWP fields can be used to characterize the spatiotemporal evolution of warm convective cloud fields. In contrast to radiances, LWP in particular has the advantage of being a physically meaningful and interpretable quantity, which is readily available as output from atmospheric models. Hence, it can offer better insights into the underlying physical processes of clouds, and is well suited for model evaluation purposes. Our results also demonstrate, however, that the observed decorrelation time depends on sensor resolution, which needs to be taken into account in such a model evaluation study.

c. Spatiotemporal characteristics of LWP fields

The relation between $\tau_{D,E}$, $\tau_{D,L}$, and the CMVs is displayed in Fig. 8 for all analyzed cases. While $\tau_{D,E}$ decays with increasing CMV, $\tau_{D,L}$ remains relatively constant, having a mean value of 31 min. The average Eulerian decorrelation time is 15.5 min. For CMVs lower than $5\,\mathrm{m\,s^{-2}}$,
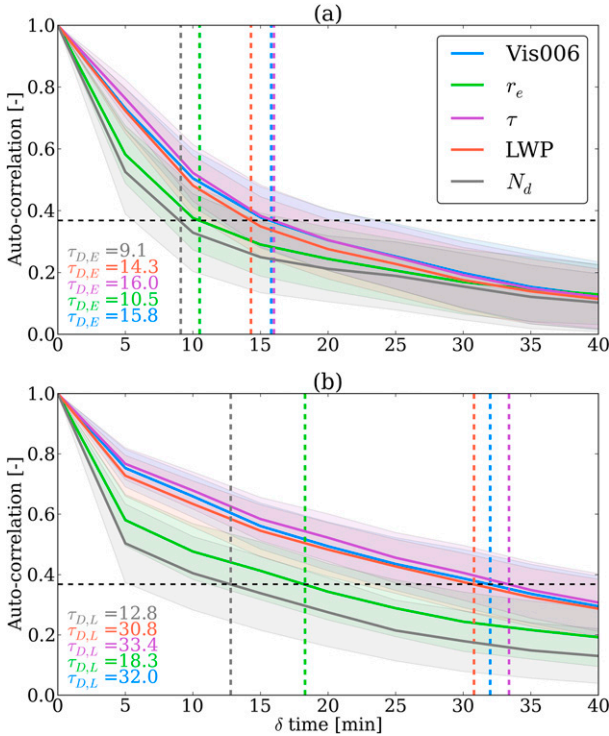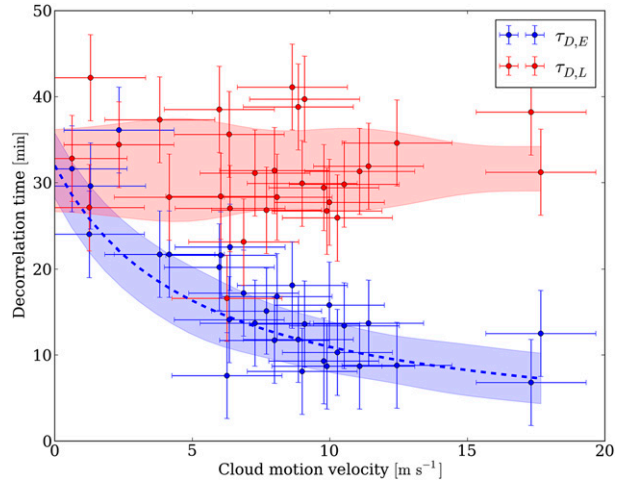
FIG. 8. Relation between the Eulerian (blue) and Lagrangian (red) decorrelation time τ_D and the CMV from MSG observations. The error bars represent the uncertainty of the CMV ($2\,\mathrm{m\,s}^{-1}$) and of τ_D (5 min), while the shaded colored areas indicate the standard deviation. The blue dashed line shows the calculated Eulerian function given by Eq. (7).

FIG. 7. As in Fig. 6, but on the basis of cloud products (r_e, τ, LWP, and N_d). The autocorrelation function of the 0.6-μm channel is added for comparison.

$\tau_{D,E}$ and $\tau_{D,L}$ are hardly distinguishable because the resulting track length is smaller than the box area, and the Eulerian and Lagrangian cloud fields strongly overlap. If the actual CMV increases above this value, $\tau_{D,E}$ drops rapidly. The strong decay in $\tau_{D,E}$ is caused by the fact that the convective cloud fields that are subsequently advected into the box are both temporally and spatially separated from the instantaneous cloud field. Thus, the advection-based change in the LWP structures is added to the internal or Lagrangian change of the LWP fields, an effect that increases with wind speed. The shaded red and blue areas indicate the standard deviation of $\tau_{D,L}$ and $\tau_{D,E}$ for a running average over different cloud motion categories.

We now assume that the statistical properties of the LWP fields are, to the first order, stationary, homogeneous, and described by Eqs. (4)–(6). As a result, the Eulerian time scale is decreased by perturbations of the spatial scales $\lambda_{D,x}$ and $\lambda_{D,y}$ that are advected by the cloud motion; that is,

$$\frac{1}{\tau_{D,E}} = \frac{1}{\tau_{D,L}} + \frac{|u|}{\lambda_{D,x}} + \frac{|v|}{\lambda_{D,y}}. \tag{7}$$

Here, u and v are the cloud motion velocities in the x and y directions, respectively. Please note that all time and space

scales are positively defined. In the limit of u and v approaching $0\,\mathrm{m\,s}^{-1}$, $\tau_{D,E}$ and $\tau_{D,L}$ become equal. In the limit of a conserved, frozen LWP structure in a Lagrangian reference frame, that is, $\tau_{D,L} \to \infty$, $\tau_{D,E}$ is solely determined by advection and only depends on u, v, $\lambda_{D,x}$, and $\lambda_{D,y}$.

The above relation (7) is shown in Fig. 8 by a dashed blue line as a function of CMV, where constant, case-average values of $\tau_{D,L} = 31$ min and $\lambda_{D,x} = 7.3$ km have been assumed. For faster CMVs, derived $\tau_{D,E}$ converge to approximately 5–10 min because of the temporal resolution constraints. A CMV uncertainty of $2\,\mathrm{m\,s}^{-1}$ is estimated from the discretization bias, which corresponds to the speed needed for one HRV pixel shift within 5 min. The uncertainty of the decorrelation time is around 5 min and has been derived from the standard deviation of $\tau_{D,L}$ across all cases.

The above relation linking Eulerian and Lagrangian time scales has important implications for the interpretation of remote sensing observations. When analyzing the temporal characteristics of a time series of ground-based observations, one has to keep in mind that the observed changes obtained from a single point measurement are always a combination of an inherent, Lagrangian temporal change, and an advective component that depends on both wind speed and a decorrelation length scale. Tracking these cloud fields in a Lagrangian reference frame allows us to separate both contributions but can be only performed with either geostationary satellite observations or a network of ground-based measurements with sufficient spatial sampling like scanning radars or cloud cameras.

Figure 9 contrasts the observed and the estimated Eulerian decorrelation times. The estimated Eulerian decorrelation time is given by the reciprocal of Eq. (7) and illustrates the link between the observed Lagrangian decorrelation time, the cloud motion velocity, and the spatial decorrelation length. The values show a rather good correlation for low decorrelation times between 10 and 20 min that are associated with high cloud motion velocities, while the spread strongly increases for high decorrelation times. The error bars of the estimated decorrelation times that are based on Gaussian error propagation even increase up to 70% for the high decorrelation times. These deviations are due to the sensor limitations of SEVIRI that lead to high tracking uncertainties especially for low cloud motions in subpixel range. However, the Pearson correlation coefficient of 0.81 demonstrates a reliable connection of the different spatiotemporal scales.

In addition to the temporal characteristics, the spatial characteristics of the cloud fields are considered by calculating the autocorrelation $R_{k,S}$ of the LWP fields as a function of distance from the actual cloud-field position. The quantities $\lambda_{D,x}$ and $\lambda_{D,y}$ are related to the typical spatial scales of LWP in the x and y directions, respectively. Averaged over all cases, $\lambda_{D,x}$ is 6.5 km and $\lambda_{D,y}$ is 8 km, with a standard deviation of 2 km for both. The difference between the two values might result from the different sensor resolutions in both directions. Figure 10 shows the relation between $\lambda_{D,x}$, $\lambda_{D,y}$, and the mean cloud diameter. The cloud diameter is determined as mean diameter of connected cloudy areas in a box referring to pixels that have a LWP higher than zero. An increase of the correlation length with increasing cloud diameter is observed. This implies that cumulus clouds lead to an even shorter decorrelation length. In contrast, we expect that much longer decorrelation lengths are obtained for more homogeneous stratocumulus cloud decks.

A statistical link between the spatial and temporal scales of cumulus cloud fields was already demonstrated by Feijt and Jonker (2000). They showed that for a cumulus and stratocumulus case, the temporal scales of a high-resolution LWP time series measured at one station could be matched to the spatial scales inferred from an LWP field obtained from a polar-orbiting satellite. The relation between correlation and distance reported here is also consistent with the findings of Slobodda et al. (2015). They report an exponential decrease of correlation with increasing distance especially for the three solar MSG channels (0.6, 0.8, and 1.6 μm), which carry information about the cloud microphysical and optical properties. Further, they concluded that correlation lengths are smaller for scenes with lower cloud coverage. The much larger
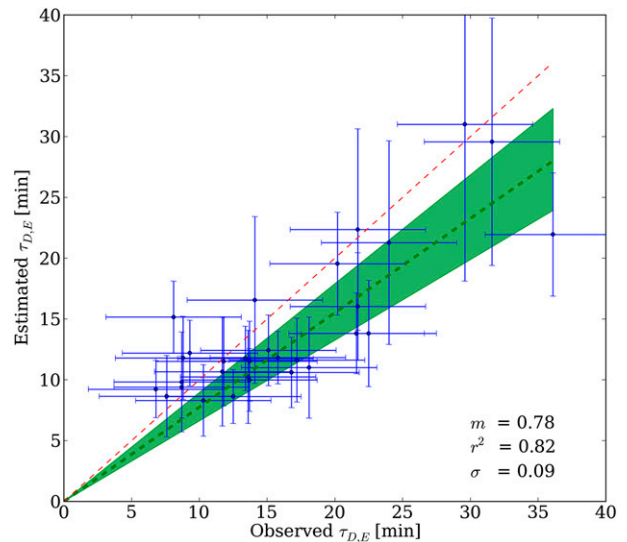

FIG. 9. Relation between the observed and estimated Eulerian decorrelation times. The estimated time connects the Lagrangian decorrelation time with the spatial decorrelation length and the cloud motion velocity according to Eq. (7). The observed average error is given as 5 min, while the estimated error results from Gaussian error propagation. The red dashed line illustrates the identity line. The green dashed line shows the linear fit function, and the surrounding shaded area spans the 5th and 95th percentiles using a bootstrap approach that indicates the error variability.

decorrelation distances reported by Slobodda et al. (2015) can result from the differences in methodology and our selection of scenes with cumulus convection. In their study, time series of fixed pixels representing ground-based measurement sites have been correlated as a function of pixel distance. We, however, apply the correlation analysis to cloud-field structures in boxes that are significantly larger than the field characteristic scales. Furthermore, the decorrelation distance and time increase strongly if the considered area is increased (Cahalan et al. 1982). For a large region over the Pacific Ocean, they found correlation lengths of up to 600 km and Lagrangian correlation time scales exceeding two days. Because of the differences in region area, methodology, and data, a comparison of our results with their reported values is not possible.

d. Temporal evolution of the cloud field-averaged LWP

The total temporal change of the box-averaged $\overline{\text{LWP}}$ is given by

$$D_t(\overline{\text{LWP}}) = \partial_t(\overline{\text{LWP}}) + \mathbf{u} \cdot \nabla(\overline{\text{LWP}}). \qquad (8)$$

Here, the total derivative $D_t(\overline{\text{LWP}})$ is given as sum of the partial derivative $\partial_t(\overline{\text{LWP}})$ and the advection of the gradient $\nabla(\overline{\text{LWP}})$ with horizontal wind speed $\mathbf{u}$.
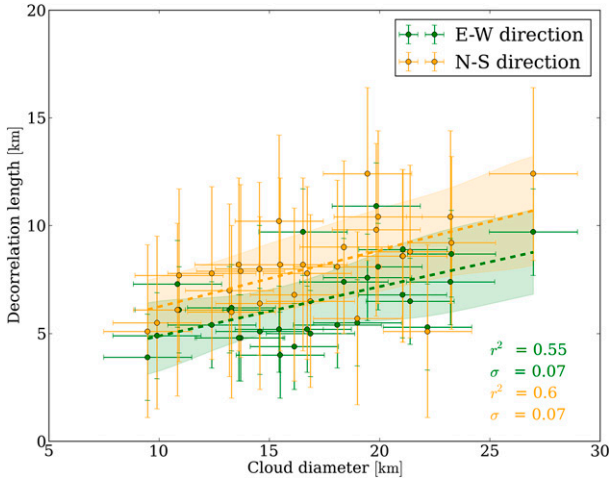
FIG. 10. Relation between the decorrelation length λ_D in the east–west (green) and north–south (orange) directions and the average cloud diameter d. The error bars represent the uncertainty of d (2 km) and λ_D (4 km), while the shaded colored areas indicate the standard deviation. The solid lines show the linear fit of both functions.

In this part of the study, we investigate the temporal change in average LWP for warm convective clouds. $\overline{\text{LWP}}$ is connected to the total mass of condensed water assuming that changes in box area and contributions from frozen hydrometeors can be neglected. Reformulating Eq. (8), a discretized version is given by

$$\Delta_t(\overline{\text{LWP}}) = \delta_t(\overline{\text{LWP}}) + u\delta_x(\overline{\text{LWP}}) + v\delta_y(\overline{\text{LWP}}), \quad (9)$$

where $\Delta_t(\overline{\text{LWP}})$, $\delta_t(\overline{\text{LWP}})$, and $\delta_{x,y}(\overline{\text{LWP}})$ denote the Lagrangian change, Eulerian change, and local spatial differences, respectively. On the one hand, if $\delta_t(\overline{\text{LWP}})$ is obtained from the Eulerian perspective, it can be directly compared with ground-based measurements. On the other hand, if we assume that $\overline{\text{LWP}}$ is affected by neither precipitation nor glaciation, $\Delta_t(\overline{\text{LWP}})$ is directly linked to evaporation and condensation within the cloud field.

The derivative $\Delta_t(\overline{\text{LWP}})$ is determined along the Lagrangian trajectory. Consequently $\Delta_t(\overline{\text{LWP}}) > 0$ implies an increase in the mass of liquid water, that is, condensation, while $\Delta_t(\overline{\text{LWP}}) < 0$ implies evaporation. The advective part is divided into two terms, the spatial change along the x direction given by $\delta_x(\overline{\text{LWP}})$ and along the y direction given by $\delta_y(\overline{\text{LWP}})$, and multiplied by the CMVs u and v, respectively. As in Eq. (7), $\Delta_t(\overline{\text{LWP}})$ and $\delta_t(\overline{\text{LWP}})$ are equal if the advective part is zero.

The time series $\Delta_t(\overline{\text{LWP}})$ and $\delta_t(\overline{\text{LWP}})$ and the total average LWP in both perspectives are shown in Fig. 11 for two exemplary cases. The bars illustrate the magnitude of the LWP change within 5 min but are scaled to
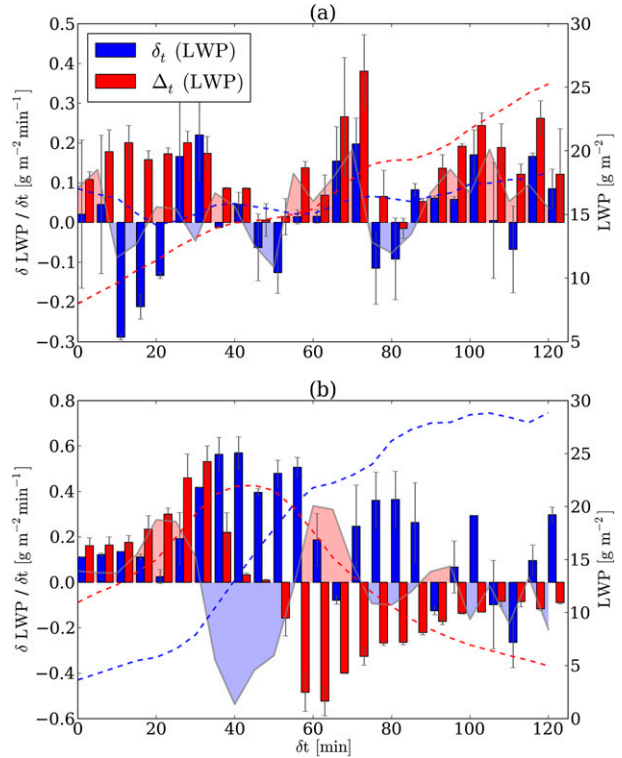

FIG. 11. Time series of the box-averaged LWP changes $\delta_t(\overline{\text{LWP}})$ and $\Delta_t(\overline{\text{LWP}})$ for the Eulerian (blue bars) and the Lagrangian (red bars) perspective, respectively. The error bars illustrate the standard deviation, and the gray line shows the absolute difference between $\Delta_t(\overline{\text{LWP}})$ and $\delta_t(\overline{\text{LWP}})$. Red shaded areas indicate $|\Delta_t(\overline{\text{LWP}})| > |\delta_t(\overline{\text{LWP}})|$, whereas blue areas indicate the opposite. The y axis on the right-hand side demonstrates the Eulerian (blue dashed line) as well as the Lagrangian (red dashed line) time series of the cloud-field average LWP. Shown are (a) case 2 and (b) case 30.

rate per minute. The right y axis represents the cloud-field-averaged LWP time series concerning the Eulerian (blue line) and the Lagrangian (red line) perspective. The shaded areas display the absolute difference between $\Delta_t(\overline{\text{LWP}})$ and $\delta_t(\overline{\text{LWP}})$. For red areas, the Lagrangian changes dominate the local tendencies. Figure 11a shows case 2 over northern Germany close to the North Sea. A cold front passed the region before the start of the track. The advection velocity was $9\,\text{m s}^{-1}$, which caused a track length of approximately 60 km. Although the boxes are overlapping for most of the track, Eulerian and Lagrangian changes are quite different. The average LWP is clearly increasing in the Lagrangian perspective, while the LWP change at a fixed location is much smaller, resulting in only a slight increase in LWP. This implies that cumulus clouds grow along their path because of condensation. However, this increase is masked to a large extent by advection in the Eulerian perspective. In contrast, case 30 (see Fig. 11b) represents an example for a rather high CMV of $18\,\text{m s}^{-1}$.

For a fixed location, the mean LWP is continuously increasing, while the tracked cloud field exhibits a different temporal evolution. A maximum $\overline{\text{LWP}}$ of around $20\,\text{g m}^{-2}$ is reached after 40 min, before it drops down again to a small value of $5\,\text{g m}^{-2}$, indicating the dissipation of the cloud field.

These two cases illustrate that the temporal changes of cloud properties are dependent on the observational perspective, and that the Lagrangian is preferable over the Eulerian perspective for a physical interpretation of governing processes. This is especially true in the presence of strong winds and large gradients in the cloud properties. The accuracy of the Lagrangian analysis is, however, affected by tracking uncertainties in addition to other uncertainties, which has to be taken into account in the interpretation of quantitative results. In the limit of low CMVs, both perspectives should converge to the same result. In our setup, however, the limited resolution of motion vectors that is fixed to multiples of the pixel resolution introduces complications for very low wind speeds.

5. Conclusions and outlook

In the present study, we have investigated the spatiotemporal evolution of warm convective cloud fields obtained from Meteosat SEVIRI observations. An advantage of Meteosat and similar geostationary satellites is their ability to monitor convective clouds and to fully resolve the cloud life cycle from the early stages of development on. We have used 30 cases of convective clouds under different synoptic conditions over central Europe as the basis of this investigation.

Solar reflectances have been used together with cloud products (HRV-CMa, CT, τ, r_e, LWP, N_d, and CMV) to characterize the spatiotemporal evolution of convective cloud fields. First, trajectories have been determined from sequences of HRV images. Boxes covering 16×16 SEVIRI standard-resolution pixels have been used to obtain an estimate of the mean properties of the convective clouds. The temporal and spatial persistence of different cloud properties has been studied with special focus on the differences between the Eulerian (i.e., fixed in space) and the Lagrangian (i.e., track following) perspectives. Assuming a Gaussian function for the autocorrelation function, which corresponds to the assumption of a first-order autoregressive process, the e-folding value has been determined as characteristic time and space scales.

The decorrelation times of SEVIRI's solar reflectances has been studied first. The decorrelation times for the 0.6-μm channel are generally larger than the decorrelation times for the 0.8-μm channel, likely because of influence of surface reflectance in particular caused by vegetation. In addition, the decorrelation of

the HRV channel at high spatial resolution ($1.2 \times 2\,\text{km}^2$) and SEVIRI standard resolution ($3.6 \times 6\,\text{km}^2$) has been compared, which has been obtained by coarse graining. The reduction in resolution results in an increase of around 3–5 min in the corresponding decorrelation times. This implies that small-scale variability in cloud structures decorrelate faster, and thus the decorrelation times are highly sensitive to the spatial resolution of the satellite sensor.

The decorrelation times of different retrieved cloud products have been determined and compared to those obtained for the reflectances. It has been found that fields of r_e and N_d exhibited much less persistence than LWP and τ, which showed comparable decorrelation times to the 0.6-μm channel. This implies that r_e and N_d are not suited as tracers for tracking. It remains unclear whether this behavior is attributable to physical reasons or is the consequence of retrieval uncertainties.

Based on our previous findings, LWP fields have been used in our further analyses, as LWP is a quantity that should be insensitive to surface heterogeneity, facilitates a process-based interpretation, and is readily available from atmospheric models and thus allows a direct comparison with model results.

The temporal evolution of box-averaged LWP was contrasted for cloud fields adopting both the Lagrangian and Eulerian perspectives. Excluding precipitation and freezing, changes in LWP in a Lagrangian reference frame are attributable to condensation and evaporation, which is essentially triggered by local convection and mixing processes. For our cases, an average decorrelation time of about 31 min has been found. The budget in an Eulerian or fixed-in-space reference frame can be significantly influenced by the advection of LWP gradients. Thus, the Eulerian decorrelation time is always lower than the Lagrangian one and depends also on the wind speed and the spatial decorrelation length scale. Typical decorrelation lengths have been found to be 6.5 km in the x direction and 8 km in the y direction. The differences between Eulerian and Lagrangian time series have been discussed for two cases.

Several sources for uncertainties have been identified that can affect the relation between the characteristic scales. The spatial decorrelation scale of 7.3 km is close to the sensor resolution of Meteosat. Furthermore, warm convective clouds often exhibit slow cloud motion velocities. This leads to uncertainties in our cloud-field tracking, because the spatial resolution of the narrowband channels and hence also the cloud properties is approximately $3.6 \times 6\,\text{km}^2$, which is coarser than the displacement of the cloud field within 5 min. To overcome this limitation and take into account subpixel shifts for an accurate estimation of spatial scales,

TABLE B1. Overview of cases including the track number, time and date of the track starting box as well as its longitude and latitude, the average CMV, the track length between the central pixel of the starting box and the central pixel of the ending box, the Eulerian ($\tau_{D,E}$) and Lagrangian ($\tau_{D,L}$) decorrelation time, and the decorrelation length in the x direction ($\lambda_{D,x}$) and y direction ($\lambda_{D,y}$).

Track	Time and date	Lon (°E)	Lat (°N)	CMV (m s^{-1})	Track length (km)	$\tau_{D,E}$ (min)	$\tau_{D,L}$ (min)	$\lambda_{D,x}$ (km)	$\lambda_{D,y}$ (km)
001	1200 UTC 14 Apr 2012	13.12	51.5	6.0	43.1	20.2	38.5	10.9	9.8
002	0930 UTC 16 Apr 2012	8.73	53.72	8.6	62.2	18.1	41.1	5.1	6.4
003	1220 UTC 16 Apr 2012	11.72	52.85	8.9	63.8	11.8	38.8	5.2	7.8
004	1220 UTC 16 Apr 2012	3.33	48.44	11.1	79.8	8.7	31.3	5	6.5
005	1340 UTC 16 Apr 2012	12.14	52.5	9.1	65.4	13.6	39.7	4.4	6.8
006	1200 UTC 21 Apr 2012	14.45	52.78	6.9	49.5	17.2	23.1	4	8.2
007	1200 UTC 21 Apr 2012	−0.68	47.44	12.4	89.6	8.8	34.6	7.4	9
008	1200 UTC 21 Apr 2012	14.37	52.39	7.7	55.4	15.1	26.8	5.2	10.2
009	1330 UTC 4 May 2012	12.1	49.7	3.8	27.5	21.7	37.3	7.3	6.1
010	1200 UTC 17 May 2012	18.54	51.53	10.3	74.0	10.3	25.9	5.5	5.7
011	1230 UTC 22 May 2012	10.69	52.59	6.4	45.9	22.5	27.0	6.1	7
012	1230 UTC 22 May 2012	11.7	51.94	6.3	45.7	14.1	35.6	6.2	6
013	1230 UTC 22 May 2012	16.66	52.57	6.3	45.1	7.6	16.6	3.9	5.1
014	1200 UTC 25 May 2012	20.14	50.75	6.0	43.5	21.6	28.4	6.8	8.6
015	1020 UTC 13 Apr 2013	3.8	50.6	10.5	75.8	13.4	29.8	8.7	9.2
016	1130 UTC 16 Apr 2013	11.47	53.56	10.0	71.9	15.8	27.7	7.6	12.4
017	1250 UTC 18 Apr 2013	7.5	52.6	17.7	127.2	12.5	31.2	8.9	8.6
018	1200 UTC 12 May 2013	3.18	49.4	9.8	70.4	9.3	29.4	7.4	10.4
019	1240 UTC 12 May 2013	9.09	51.35	9.0	64.8	8.1	29.9	9.7	12.4
020	1240 UTC 12 May 2013	5.94	47.49	8.0	57.5	11.7	31.4	5.3	5.1
021	1140 UTC 15 May 2013	0.78	48.84	11.4	82.2	13.7	31.9	6.5	8.8
022	1250 UTC 15 May 2013	−0.68	47.44	9.9	71.3	8.7	26.7	5.4	8.1
023	1150 UTC 19 May 2013	18.3	52.67	7.3	52.4	13.7	31.1	4.8	7.9
024	1230 UTC 19 May 2013	18.6	52.5	8.1	58.2	16.8	28.3	4.8	8.2
025	1250 UTC 19 May 2013	14.47	51.92	4.2	30.0	21.7	28.3	6.1	7.7
026	1100 UTC 8 Jun 2013	5.51	49.34	2.3	16.8	36.1	34.4	8.1	10.4
027	1100 UTC 8 Jun 2013	9.645	51.2	0.6	4.5	31.6	32.8	8	8
028	1300 UTC 8 Jun 2013	9.92	48.3	1.3	9.1	24.0	27.1	4.9	5.5
029	1300 UTC 8 Jun 2013	9.5	48.8	1.3	9.4	29.6	42.2	5.4	7.8
030	1250 UTC 15 Jun 2013	5.82	52.32	17.3	124.7	6.8	38.2	9.7	8.2

the use of the HRV channel with a threefold higher spatial resolution is essential.

This study demonstrates that the spatiotemporal characterization of warm convective clouds is currently limited by the spatial sensor resolution of Meteosat. Carbajal Henken et al. (2011) already found that SEVIRI's standard resolution is not sufficient to fully resolve the small-scale spatial variability required for the identification of warm convective clouds, and used an estimate of τ based on the HRV channel. The additional use of the HRV channel can thus not only improve the tracking accuracy (Zinner et al. 2008), but can also help to better resolve small-scale cloud variability. A successful application of the HRV reflectances to improve the spatial resolution of narrowband images was presented by Deneke and Roebeling (2010). Bley and Deneke (2013) developed an HRV-CMa to improve the detection of small-scale convective clouds. The HRV channel was further applied to sharpen partly cloudy IR satellite pixels for improving convective initiation detection schemes (Mecikalski et al. 2013).

These studies support the concept that the HRV channel can help to overcome the limitations due to SEVIRI's standard spatial resolution noted in this work. Within the framework of the Germany-wide research initiative High Definition Clouds and Precipitation for Climate Prediction [HD(CP)^2] (Dipankar et al. 2015), the authors are therefore currently developing a cloud property retrieval based on the HRV channel, which includes downscaled cloud properties (τ, r_e, and LWP). Future plans also include the application of the spatiotemporal analysis presented here to the high-resolution simulations of icosahedral nonhydrostatic (ICON)-LES, which cover Germany with a horizontal resolution of 150 m.

The analysis demonstrates the advantage of the Lagrangian perspective for studying convective and advective processes that are influenced by cloud variability. These results should be considered in future modeling studies to evaluate and improve stochastic parameterizations of cumulus convection. Further comparisons of the spatiotemporal characteristics of convective clouds with high-resolution model results are essential to better understand and reduce their uncertainties.

On the one hand, the methods used in this investigation can serve as basis for an evaluation of the realistic

representation of clouds in ICON-LES including their spatiotemporal behavior. On the other hand, the high resolution of the model runs enable a quantification of the resolution dependence of the temporal and spatial scales determined in this article, and can thus help to quantify the information gains expected from future geostationary satellites such as Meteosat Third Generation with improved spatial and temporal resolutions. It will have a 10-min standard repeat cycle for the full disk (Stuhlmann et al. 2005) and an improved spatial resolution of 1 km for all solar channels, which will offer the great opportunity to investigate the temporal evolution of cumulus cloud fields over other relevant climatic regions (e.g., the Atlantic warm pool) using the techniques introduced here.

APPENDIX A

Configuration of the HRW Tools

The configuration file of the HRW product has been adapted to obtain more tracers especially for small cumulus structures with low reflectance values. This could be realized by considering more tracers for the vector calculation even for a slightly smaller quality threshold. More details can be found in the configuration text file that is available in the online supplemental material.

APPENDIX B

Overview of Cases

Table B1 gives an overview of all analyzed cases including the track identification number, date and time of the track starting box as well as its longitude and latitude, the average CMV, the track length between the central pixel of the starting box and the central pixel of the ending box, the Eulerian ($\tau_{D,E}$) and Lagrangian ($\tau_{D,L}$) decorrelation time, and the decorrelation length in the x ($\lambda_{D,x}$) and y ($\lambda_{D,y}$) directions.

REFERENCES

Albrecht, B. A., 1989: Aerosols, cloud microphysics, and fractional cloudiness. *Science*, **245**, 1227–1230, doi:10.1126/science.245.4923.1227.

Bedka, K. M., and J. R. Mecikalski, 2005: Application of satellite-derived atmospheric motion vectors for estimating mesoscale flows. *J. Appl. Meteor.*, **44**, 1761–1772, doi:10.1175/JAM2264.1.

Bley, S., and H. Deneke, 2013: A threshold-based cloud mask for the high-resolution visible channel of Meteosat Second Generation SEVIRI. *Atmos. Meas. Tech.*, **6**, 2713–2723, doi:10.5194/amt-6-2713-2013.

Brenguier, J.-L., H. Pawlowska, L. Schüller, R. Preusker, J. Fischer, and Y. Fouquart, 2000: Radiative properties of boundary layer clouds: Droplet effective radius versus number concentration. *J. Atmos. Sci.*, **57**, 803–821, doi:10.1175/1520-0469(2000)057<0803:RPOBLC>2.0.CO;2.

Brown, A., and Coauthors, 2002: Large-eddy simulation of the diurnal cycle of shallow cumulus convection over land. *Quart. J. Roy. Meteor. Soc.*, **128**, 1075–1093, doi:10.1256/003590002320373210.

Cahalan, R. F., D. A. Short, and G. R. North, 1982: Cloud fluctuation statistics. *Mon. Wea. Rev.*, **110**, 26–43, doi:10.1175/1520-0493(1982)110<0026:CFS>2.0.CO;2.

Carbajal Henken, C., M. J. Schmeits, H. Deneke, and R. A. Roebeling, 2011: Using MSG-SEVIRI cloud physical properties and weather radar observations for the detection of Cb/TCu clouds. *J. Appl. Meteor. Climatol.*, **50**, 1587–1600, doi:10.1175/2011JAMC2601.1.

Clement, A. C., R. Burgman, and J. R. Norris, 2009: Observational and model evidence for positive low-level cloud feedback. *Science*, **325**, 460–464, doi:10.1126/science.1171255.

Coakley, J. A., M. A. Friedman, and W. R. Tahnk, 2005: Retrieval of cloud properties for partly cloudy imager pixels. *J. Atmos. Oceanic Technol.*, **22**, 3–17, doi:10.1175/JTECH-1681.1.

Davis, A., A. Marshak, W. Wiscombe, and R. Cahalan, 1996: Scale invariance of liquid water distributions in marine stratocumulus. Part I: Spectral properties and stationarity issues. *J. Atmos. Sci.*, **53**, 1538–1558, doi:10.1175/1520-0469(1996)053<1538:SIOLWD>2.0.CO;2.

Deneke, H. M., and R. A. Roebeling, 2010: Downscaling of Meteosat SEVIRI 0.6 and 0.8 μm channel radiances utilizing the high-resolution visible channel. *Atmos. Chem. Phys.*, **10**, 9761–9772, doi:10.5194/acp-10-9761-2010.

——, W. H. Knap, and C. Simmer, 2009: Multiresolution analysis of the temporal variance and correlation of transmittance and reflectance of an atmospheric column. *J. Geophys. Res.*, **114**, D17206, doi:10.1029/2008JD011680.

Derrien, M., and H. Le Gléau, 2005: MSG/SEVIRI cloud mask and type from SAFNWC. *Int. J. Remote Sens.*, **26**, 4707–4732, doi:10.1080/01431160500166128.

Dipankar, A., B. Stevens, R. Heinze, C. Moseley, G. Zängl, M. Giorgetta, and S. Brdar, 2015: Large eddy simulation using the general circulation model ICON. *J. Adv. Model. Earth Syst.*, **7**, 963–986, doi:10.1002/2015MS000431.

Dorrestijn, J., D. T. Crommelin, A. P. Siebesma, and H. J. J. Jonker, 2013: Stochastic parameterization of shallow cumulus convection estimated from high-resolution model data. *Theor. Comput. Fluid Dyn.*, **27**, 133–148, doi:10.1007/s00162-012-0281-y.

Feijt, A., and H. Jonker, 2000: Comparison of scaling parameters from spatial and temporal distributions of cloud properties. *J. Geophys. Res.*, **105**, 29 089–29 097, doi:10.1029/2000JD900414.

García-Pereda, J., 2013: High resolution winds (HRW—PGE09 v4.0). Algorithm Theoretical Basis Doc. SAF/NWC/CDOP/INM/SCI/ATBD/09, 78 pp. [Available online at http://www.nwcsaf.org/HTMLContributions/SUM/SAF-NWC-CDOP2-INM-SCI-ATBD-09_v4.0.pdf.]

Hammer, A., D. Heinemann, E. Lorenz, and B. Lückehe, 1999: Short-term forecasting of solar radiation: A statistical approach using satellite data. *Sol. Energy*, **67**, 139–150, doi:10.1016/S0038-092X(00)00038-4.

Han, Q., W. B. Rossow, and A. A. Lacis, 1994: Near-global survey of effective droplet radii in liquid water clouds using ISCCP data. *J. Climate*, **7**, 465–497, doi:10.1175/1520-0442(1994)007<0465:NGSOED>2.0.CO;2.

Horvath, A., C. Seethala, and H. Deneke, 2014: View angle dependence of MODIS liquid water path retrievals in warm oceanic clouds. *J. Geophys. Res.*, **119**, 8304–8328, doi:10.1002/2013JD021355.

Jonkheid, B. J., R. A. Roebeling, and E. van Meijgaard, 2012: A fast SEVIRI simulator for quantifying retrieval uncertainties in the CM SAF cloud physical property algorithm. *Atmos. Chem. Phys.*, **12**, 10 957–10 969, doi:10.5194/acp-12-10957-2012.

Koren, I., L. Oreopoulos, G. Feingold, L. A. Remer, and O. Altaratz, 2008: How small is a small cloud? *Atmos. Chem. Phys.*, **8**, 3855–3864, doi:10.5194/acp-8-3855-2008.

Lenderink, G., and Coauthors, 2004: The diurnal cycle of shallow cumulus clouds over land: A single-column model intercomparison study. *Quart. J. Roy. Meteor. Soc.*, **130**, 3339–3364, doi:10.1256/qj.03.122.

Lensky, I. M., and D. Rosenfeld, 2008: Clouds-Aerosols-Precipitation Satellite Analysis Tool (CAPSAT). *Atmos. Chem. Phys.*, **8**, 6739–6753, doi:10.5194/acp-8-6739-2008.

Marshak, A., S. Platnick, T. Várnai, G. Wen, and R. F. Cahalan, 2006: Impact of three-dimensional radiative effects on satellite retrievals of cloud droplet sizes. *J. Geophys. Res.*, **111**, D09207, doi:10.1029/2005JD006686.

Mecikalski, J. R., M. Koenig, and C. P. Jewett, 2013: Application of high-resolution visible sharpening of partly cloudy pixels in Meteosat Second Generation infrared imagery. *Atmos. Res.*, **134**, 1–11, doi:10.1016/j.atmosres.2013.07.014.

Nakajima, T., and M. D. King, 1990: Determination of the optical thickness and effective particle radius of clouds from reflected solar radiation measurements. Part I: Theory. *J. Atmos. Sci.*, **47**, 1878–1893, doi:10.1175/1520-0469(1990)047<1878:DOTOTA>2.0.CO;2.

Nicholls, S., and J. Leighton, 1986: An observational study of the structure of stratiform cloud sheets: Part I. Structure. *Quart. J. Roy. Meteor. Soc.*, **112**, 431–460, doi:10.1002/qj.49711247209.

Quaas, J., O. Boucher, and U. Lohmann, 2006: Constraining the total aerosol indirect effect in the LMDZ and ECHAM4 GCMs using MODIS satellite data. *Atmos. Chem. Phys.*, **6**, 947–955, doi:10.5194/acp-6-947-2006.

Roebeling, R. A., A. J. Feijt, and P. Stammes, 2006: Cloud property retrievals for climate monitoring: Implications of differences between Spinning Enhanced Visible and Infrared Imager (SEVIRI) on *Meteosat-8* and Advanced Very High Resolution Radiometer (AVHRR) on *NOAA-17*. *J. Geophys. Res.*, **111**, D20210, doi:10.1029/2005JD006990.

——, H. M. Deneke, and A. J. Feijt, 2008: Validation of cloud liquid water path retrievals from SEVIRI using one year of CloudNET observations. *J. Appl. Meteor. Climatol.*, **47**, 206–222, doi:10.1175/2007JAMC1661.1.

Rossow, W. B., and L. C. Garder, 1993: Cloud detection using satellite measurements of infrared and visible radiances for ISCCP. *J. Climate*, **6**, 2341–2369, doi:10.1175/1520-0442(1993)006<2341:CDUSMO>2.0.CO;2.

Schmetz, J., P. Pili, S. Tjemkes, D. Just, J. Kerkmann, S. Rota, and A. Ratier, 2002: An introduction to Meteosat Second Generation (MSG). *Bull. Amer. Meteor. Soc.*, **83**, 977–992, doi:10.1175/1520-0477(2002)083<0977:AITMSG>2.3.CO;2.

Schulz, J., and Coauthors, 2009: Operational climate monitoring from space: the EUMETSAT Satellite Application Facility on Climate Monitoring (CM-SAF). *Atmos. Chem. Phys.*, **9**, 1687–1709, doi:10.5194/acp-9-1687-2009.

Senf, F., F. Dietzsch, A. Hünerbein, and H. Deneke, 2015: Characterization of initiation and growth of selected severe convective storms over central Europe with MSG-SEVIRI. *J. Appl. Meteor. Climatol.*, **54**, 207–224, doi:10.1175/JAMC-D-14-0144.1.

Slobodda, J., A. Hünerbein, R. Lindstrot, R. Preusker, K. Ebell, and J. Fischer, 2015: Multichannel analysis of correlation length of SEVIRI images around ground-based cloud observatories to determine their representativeness. *Atmos. Meas. Tech.*, **8**, 567–578, doi:10.5194/amt-8-567-2015.

Stuhlmann, R., A. Rodriguez, S. Tjemkes, J. Grandell, A. Arriaga, J.-L. Bézy, D. Aminou, and P. Bensi, 2005: Plans for EUMETSAT's Third Generation Meteosat geostationary satellite programme. *Adv. Space Res.*, **36**, 975–981, doi:10.1016/j.asr.2005.03.091.

Trenberth, K. E., J. T. Fasullo, and J. Kiehl, 2009: Earth's global energy budget. *Bull. Amer. Meteor. Soc.*, **90**, 311–323, doi:10.1175/2008BAMS2634.1.

Turner, D. D., and Coauthors, 2007: Thin liquid water clouds: Their importance and our challenge. *Bull. Amer. Meteor. Soc.*, **88**, 177–190, doi:10.1175/BAMS-88-2-177.

Von Storch, H., and F. W. Zwiers, 2002: *Statistical Analysis in Climate Research*. Cambridge University Press, 496 pp.

Wolters, E. L. A., H. M. Deneke, B. J. J. M. van den Hurk, J. F. Meirink, and R. A. Roebeling, 2010: Broken and inhomogeneous cloud impact on satellite cloud particle effective radius and cloud-phase retrievals. *J. Geophys. Res.*, **115**, D10214, doi:10.1029/2009JD012205.

Wood, R., and D. L. Hartmann, 2006: Spatial variability of liquid water path in marine low cloud: The importance of mesoscale cellular convection. *J. Climate*, **19**, 1748–1764, doi:10.1175/JCLI3702.1.

Zinner, T., and B. Mayer, 2006: Remote sensing of stratocumulus clouds: Uncertainties and biases due to inhomogeneity. *J. Geophys. Res.*, **111**, D14209, doi:10.1029/2005JD006955.

——, H. Mannstein, and A. Tafferner, 2008: Cb-TRAM: Tracking and monitoring severe convection from onset over rapid development to mature phase using multi-channel *Meteosat-8* SEVIRI data. *Meteor. Atmos. Phys.*, **101**, 191–210, doi:10.1007/s00703-008-0290-y.